Accelerated Weak Signal Search Using Mode Entanglement and State Swapping

Y. Jiang[®], ^{1,2,†} E.P. Ruddy[®], ^{1,2,†} K.O. Quinlan[®], ^{1,2} M. Malnou[®], ³ N.E. Frattini[®], ^{1,2} and K.W. Lehnert 1,2,*

¹JILA, National Institute of Standards and Technology and the University of Colorado Boulder, Boulder, Colorado 80309, USA

²Department of Physics, University of Colorado Boulder, Boulder, Colorado 80309, USA ³ National Institute of Standards and Technology, Boulder, Colorado 80305, USA

(Received 15 November 2022; accepted 2 March 2023; published 6 April 2023)

Quantum fluctuations constitute the primary noise barrier limiting cavity-based axion-dark-matter searches. In an experiment designed to mimic a real axion search, we employ a quantum enhanced sensing technique to detect a synthetic axionlike microwave tone at an unknown frequency weakly coupled to a resonator, demonstrating a factor-of-5.6 acceleration relative to a quantum limited search for the same tone. This speed-up is achieved by dynamically coupling the resonator mode to a second (readout) mode with balanced swapping and two-mode squeezing interactions, which results in both visibility-bandwidth and peak-visibility increase. A small fractional imbalance between the two interaction rates yields further scan-rate enhancement and we demonstrate that an eightfold acceleration can be achieved.

DOI: 10.1103/PRXQuantum.4.020302

I. INTRODUCTION

Ouantum fluctuations intrinsic to the measurement of the electromagnetic field of a cavity [1] are a major source of background noise in searches for weak signals [2–4]. As the main source of background in cavity-based axion searches [5,6], they are the primary limitation inhibiting a comprehensive search of the axion parameter space. The figure of merit for cavity-based axion detectors (haloscopes) is the spectral scan rate. This is defined as the rate at which a search can scan through frequency space while probing with sufficient confidence to resolve or exclude an axion with a given coupling to electromagnetism. It would take thousands of years for existing quantum limited haloscopes to scan the (1-10)-GHz frequency band at benchmark Dine-Fischler-Srednicki-Zhitnitsky (DFSZ) coupling [7-9].

The scan rate depends on two quantities: the characteristic axion-sensitive bandwidth (visibility bandwidth) of the detector and the peak visibility of a potential axion signal. Quantum enhanced sensing techniques hold promise for increasing these quantities and for facilitating the otherwise prohibitively time- and resource-expensive

Published by the American Physical Society under the terms of the Creative Commons Attribution 4.0 International license. Further distribution of this work must maintain attribution to the author(s) and the published article's title, journal citation, and DOI.

search. Recently, squeezing has been implemented in an axion search, doubling detector scan rate relative to a search at the quantum limit [10,11]. In that experiment, one quadrature of the measurement-induced noise has been squeezed below the level of vacuum fluctuations, thereby accelerating the search by widening the axion-sensitive bandwidth of the haloscope. The achievement of further scan-rate enhancement with this technique is challenging due to limitations associated with transporting fragile squeezed states through lossy directional elements in the measurement chain [11].

In this paper, we demonstrate a method of scan-rate enhancement that circumvents the main limitation of the squeezing technique and achieves both further bandwidth increase and peak-visibility improvement, enabling a factor-of-5.6 acceleration in the detection of a synthetic axionlike microwave tone. Rather than squeezing the measurement noise, this method depends on amplifying a potential axion signal before it is polluted by measurement noise: an interaction that is enabled by carefully balancing entanglement and swapping interactions between a resonator (cavity) mode and an auxiliary readout mode [12]. To characterize the performance of this quantum enhanced technique, we perform a realistic acquisition and processing protocol to detect a weak synthetic axionlike microwave tone that has a power spectral density (PSD) that is approximately 1% of the PSD expected from vacuum fluctuations. By operating the detector with and without the quantum enhancement enabled, we demonstrate a factor-of-2.36 improvement in the signal-to-noise ratio (SNR) with the same measurement

^{*}konrad.lehnert@jila.colorado.edu

[†]These two authors contributed equally

time, corresponding to a 5.6-fold speed-up over the quantum limited haloscope. Furthermore, we demonstrate additional scan-rate enhancement by imbalancing the parametric interactions slightly [13,14] which enables greater interaction rates and a bandwidth increase. We show that an eightfold acceleration is achievable with this modification. Further scan-rate enhancement, around 20-fold, should be achievable in applications of this technique to a real axion search.

In Sec. II, we summarize the key features of the quantum enhanced method. In Sec. III, we describe the prototype device used in this demonstration experiment and we characterize its performance. In Sec. IV, we apply the quantum enhanced method based on balanced interactions to the search for a weak axionlike microwave tone at an unknown frequency and we extract the scan-rate enhancement. Finally, in Sec. V, we demonstrate additional scan-rate enhancement using the imbalanced method.

II. QUANTUM ENHANCED BANDWIDTH AND VISIBILITY IMPROVEMENT

The scan rate of an axion search is limited by vacuum fluctuations arising from both the internal loss of the cavity and the loss external to the cavity. To understand their relative contributions to the scan rate, we consider the effects of these two noise sources as measured at the input of the measurement chain. The internal loss of the cavity (with loss rate κ_f) induces cavity noise, which is maximal on cavity resonance. A potential axion signal, which is weakly coupled to the cavity at a rate κ_a , follows the same path through the haloscope as does the cavity noise, as illustrated in Fig. 1(a). Therefore, the ratio of the axion-signal PSD to the cavity noise PSD is κ_a/κ_f over the entire spectrum. Measurement noise, arising from loss external to the cavity, dominates off resonance. The relative spectral contributions of the signal and noise sources are illustrated in Fig. 1(b). We define the visibility α as the ratio of PSD resulting from a potential axion field to the total noise PSD and the visibility bandwidth $L'l_{\alpha}$ as the bandwidth over which the level of cavity noise dominates over the level of measurement noise.

Noiselessly amplifying the cavity noise and potential axion signal together relative to the level of measurement noise increases the visibility bandwidth, as illustrated in Fig. 1(d) [12]. The amplification also results in peak-visibility increase, further enhancing the scan rate, as is discussed in Sec. III and Appendix A. Ideally, the amplification of the cavity noise and axion signal would

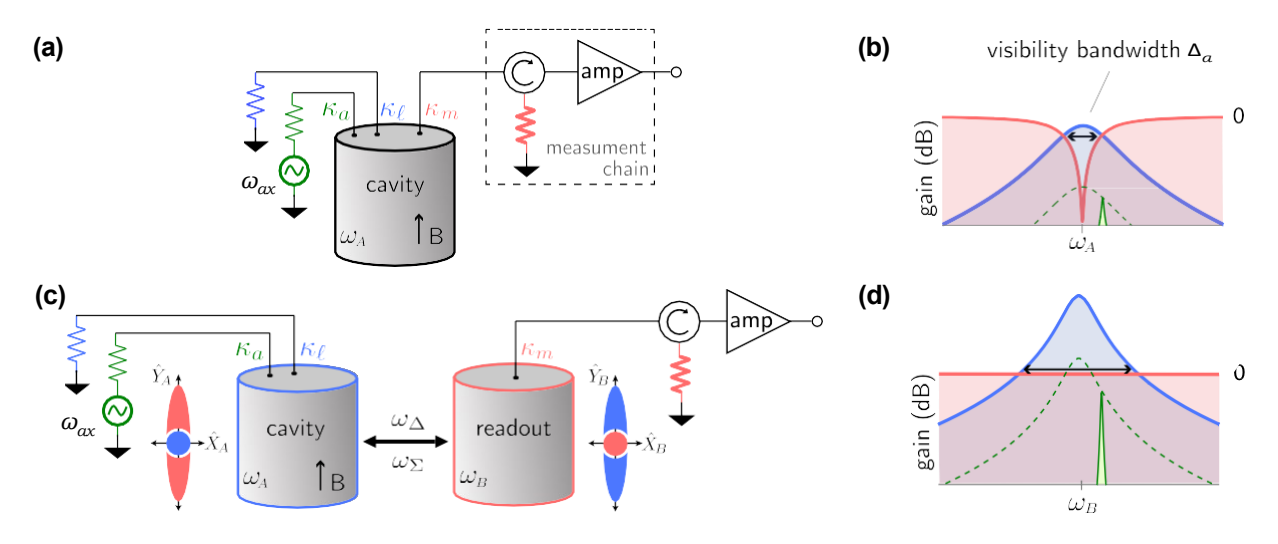


FIG. 1. A comparison between a quantum limited haloscope and a GC-enhanced haloscope. (a) A microwave network model for a quantum limited haloscope. The axion signal, modeled by a generator at frequency ω_{ax} , and the cavity loss, modeled by the blue resistor, are coupled to a cavity centered at ω_A through fictitious ports at rates κ_a and κ_f . The outgoing cavity fields couple to the measurement chain at a rate κ_m and are routed by a circulator toward a near-noiseless amplifier (amp). The circulator shields the cavity from amplifier backaction by dissipating the backaction at a physical termination (bold red resistor). Vacuum noise (measurement noise) sourced from that termination is reflected off the cavity measurement port and couples to the measurement chain, polluting the axion signal. (b) The spectral distribution with respect to vacuum fluctuations of the cavity noise (blue), measurement noise (red), and axion signal (green) at the input of the measurement chain of a quantum limited haloscope. The green dashed line represents the response to an axion signal at any given frequency, while the narrow green peak represents a potential manifestation of the narrowband axion signal. (c) A microwave network model and phase-space diagram for the GC-enhanced haloscope. The measured quadrature, \hat{Y}_B , contains amplified axion signal and cavity noise and vacuum-level measurement noise, where the size of the fluctuations in the quadrature amplitudes is represented by the blue ellipse and red circle in phase space. (d) At the input of the measurement chain, signal visibility is preserved over a wider bandwidth due to the amplification of the cavity noise and potential axion signal relative to the vacuum-level measurement noise. In contrast to the quantum limited case, the measurement noise does not vanish on resonance as a result of the balanced parametric interactions.

occur inside the axion-photon conversion cavity and the amplified fields could be measured directly. However, the magnetic field that enables the axion-photon conversion [5] is incompatible with the superconducting circuit elements capable of performing the noiseless amplification. Therefore, the cavity noise and potential axion signal must be transported from the cavity mode (A) to an auxiliary readout mode (B) and amplified there, as depicted in Fig. 1(c).

The two-cavity amplification is achieved by a quantum nondemolition (QND) interaction resulting from two drives. A state-swapping interaction at a rate g_C , induced by a frequency-conversion drive (C) at the difference of the two mode frequencies, $\omega_{L} = \omega_A \omega_B$, is used to continuously exchange the states of the cavity and readout modes. A two-mode squeezing (entanglement) interaction at a rate g_G , induced by driving at the sum of the two mode frequencies, $\omega_{:E} = \omega_A \ \omega_B$, enables gain (G) and quadrature correlations between the cavity and readout modes [15,16]. Applying the two drives simultaneously and balancing their interaction rates, $g_C = g_G$, results in a QND interaction given by $\hat{H}_{GC} = 2g_C \hat{X}_A \hat{X}_B$ [12], which causes the fields from the cavity-mode quadrature X_A to be amplified noiselessly at the orthogonal quadrature of the readout mode \hat{Y}_B , while \hat{X}_A itself remains unchanged, as shown in the phase-space diagram in Fig. 1(c). Thus, we can extract the information contained in X_A by measuring Y_B and the lack of backaction on X_A enables a faster measurement rate compared to that of a quantum limited haloscope, resulting in bandwidth increase, as shown in Fig. 1(d). In the following sections, we refer to this type of quantum enhanced method as the GC-enhanced method.

III. DEMONSTRATION OF BANDWIDTH AND VISIBILITY IMPROVEMENT

In order to experimentally test the GC-enhanced method, we operate a Josephson parametric converter (JPC) [17,18] as a prototype device in a way that mimics a haloscope. The JPC, as illustrated in Fig. 2(a), comprises two half-wave microstrip resonators, each formed by a pair of quarter-wave strips, coupled by a Josephson ring modulator (JRM), which serves as the three-wave mixing element that enables the swapping and two-mode squeezing interactions. The JPC has three electrical eigenmodes that participate in the JRM: two differential modes that constitute the cavity and readout modes and a common mode that is used to apply the ω_{LT} and $\omega_{:E}$ drives that induce the QND interaction [12,19,20]. The cavity mode, which is held at a fixed frequency around $\omega_A/2\pi = 7.454$ GHz in this proto type experiment, has an internal loss rate of $\kappa / 2\pi =$ 960 + 15 kHz and is weakly coupled to an external port at a rate $\kappa_a/2\pi$ =1220 ±20 Hz. This port is accessed via the differential port of a 180° hybrid coupler, the two outputs of which oscillate in antiphase to excite the cavity

mode. It is used to introduce probe tones produced by a microwave generator into the resonator for visibility characterization. The readout mode at $\omega_B/2\pi = 4.989$ GHz is strongly coupled at a rate $\kappa_m/2\pi = 20.6 \pm 1.3$ MHz to the measurement chain through the differential port of another hybrid coupler. The sum port of the same hybrid coupler is used to excite the common mode of the JPC and thus to activate the entanglement and swapping interactions. The JPC is thermally connected to the base plate of a dilution refrigerator that has an operation temperature of 20 mK. Further details on the experimental setup are included in Appendix B.

We operate the JPC under two conditions to demonstrate the visibility-bandwidth and peak-visibility improvements: one that operates at a quantum limited scan rate and one that applies the GC enhancement. Here, we refer to the quantum limited scan rate as the maximum achievable scan rate of a critically coupled haloscope with only vacuum fluctuations entering at its loss and measurement ports and that can measure both quadratures of the field exiting the cavity with the minimum required added noise or, equivalently, can measure a single quadrature noiselessly [1]. To achieve this benchmark quantum limited performance, we apply only the conversion drive (C) to the JPC, thus using it to mimic a single cavity with an effective measurement port coupling rate $\kappa_{m,\text{eff}} = 4g_C^2/\kappa_m$. This approximation is valid in the well-satisfied limit $\kappa_{k \leftarrow} \kappa_m$. For quantum limited operation, the effective single cavity simulated by the JPC is critically coupled such that $\kappa_{m,\text{eff}} =$

 κ_f . This is achieved by setting $g_C = \sqrt{\kappa_m \kappa_f}/2$. Experimentally, this operating point is located by measuring $|S_{mm}(\delta)|$ As $|S_{mm}(0)| \to 0$, the interaction rate approaches $g_C = \sqrt{\kappa_m \kappa_f}/2$. To operate in the GC-enhanced mode, both the swapping and two-mode squeezing drives are applied at their largest achievable rates before the GC performance becomes unstable, as described in Sec. IV $(g_C/2\pi = g_G/2\pi - 2.30 - 0.05)$ MHz for this device). In both cases, near-noiseless readout is achieved by directing the output of the JPC to a near-noiseless flux-pumped Josephson parametric amplifier (JPA) [21–24] which is operated phase sensitively such that in the GC-enhanced case, it is phase locked to the JPC (see Appendix B) and amplifies the JPC-amplified quadrature.

We first demonstrate visibility-bandwidth increase by measuring the scattering parameters of the JPC in both transmission and reflection. Although there is no accessible port associated with the internal loss of the cavity, the scattering parameter for the cavity noise in transmission, $|S_{mf}|$, may be inferred from the axion-signal scattering parameter $|S_{mq}|$ with $|S_{mf}| = \overline{\kappa_f/\kappa_a}|S_{ma}|$. We observe unit transmission of the cavity noise on resonance in the quantum limited case [blue in Fig. 2(b)] and 16 dB of phase-preserving gain, corresponding with 22 dB of phase-sensitive gain, in the GC-enhanced case [Fig. 2(c)]. Measuring in reflection off the measurement port, $|S_{mm}|$,

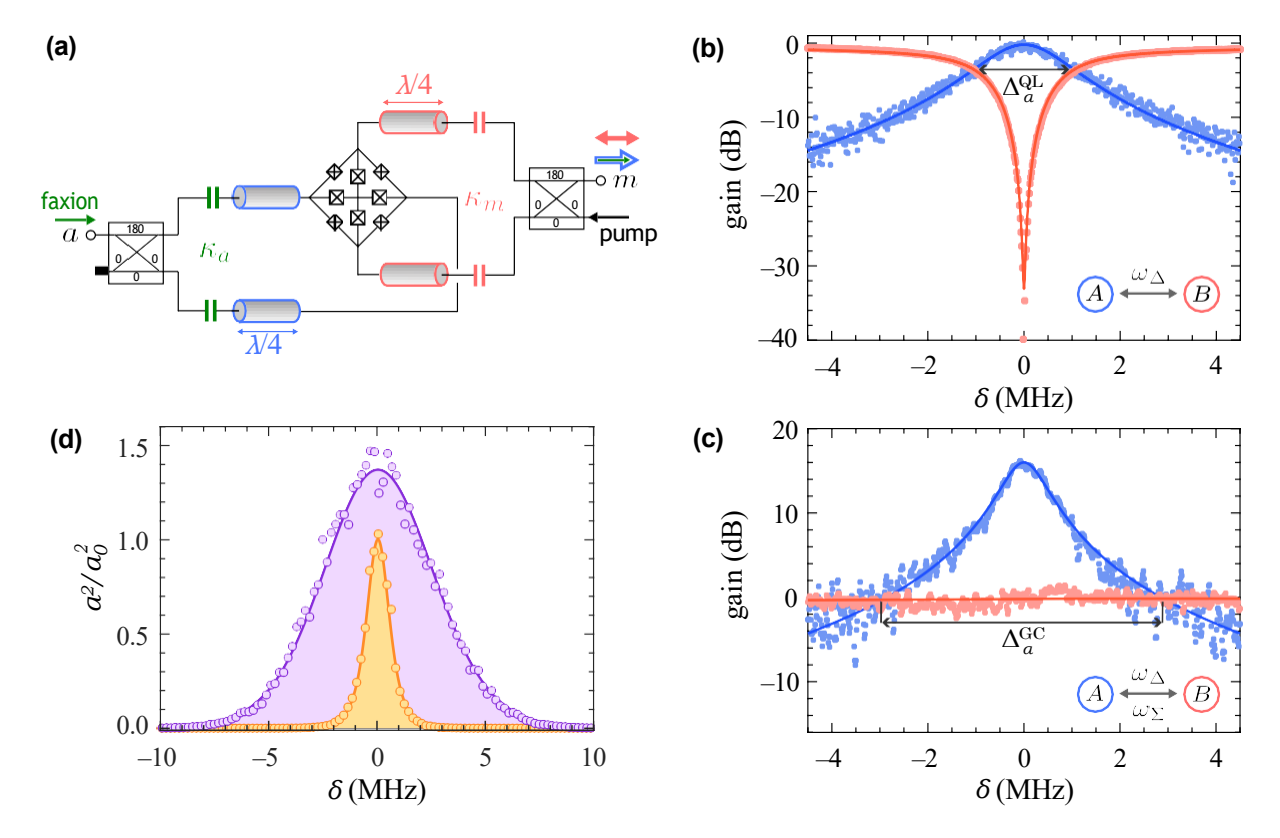


FIG. 2. An experimental demonstration of visibility-bandwidth increase. (a) The circuit diagram of a Josephson parametric converter (JPC). The cavity mode (blue) is accessed through the axion port (a) and the readout mode (red) is accessed through the measurement port (m). (b) The gain of the cavity noise (blue) and measurement noise (red) at the measurement port of the JPC as a function of detuning (δ) from the point of unit transmission as measured at the readout port under quantum limited operation ($g_C = \sqrt[N]{\kappa_m \kappa_y/2}$). Fits from the system scattering parameters $|S_{mf}|^2$ and $|S_{mm}|^2$ as derived from Appendix A are included as solid lines. (c) The gain from GC-enhanced operation ($g_C = g_G$), plotted as a function of the detuning (δ) from the point of peak transmission. The cavity noise is amplified while the measurement noise is reflected with unit magnitude, resulting in visibility-bandwidth increase ($L'I^{GC}_{\alpha} > L'I^{QL}_{\alpha}$). Fits are included as solid lines, from which we extract the fitting parameters $g_C/2\pi = g_G/2\pi = 7.30 \pm 0.05$ MHz. (d) The visibility squared (α^2) for the quantum limited (orange) and GC-enhanced (purple) cases. In both cases, α^2 is normalized to the peak value $\alpha^2(0)$ of the quantum limited case. A scan-rate enhancement of 5.69 ± 0.12 is extracted from the ratio of the areas enclosed by the purple and orange curves.

we observe near-zero reflection on resonance in the quantum limited case [red in Fig. 2(b)] as a result of critically coupling $(\kappa_{m,\text{eff}} = \kappa_f)$ and we observe unit reflection over the entire bandwidth in the GC-enhanced case [Fig. 2(c)] as a result of the matched interaction rates $g \in g_G$. The gain experienced by the cavity noise relative to the level of measurement noise in the GC-enhanced case results in a wider visibility bandwidth compared with the quantum limited bandwidth $(L'_{\alpha}^{GC} > L'_{\alpha}^{QL})$, as marked by the black arrows.

The other advantage of the GC-enhanced technique, the peak-visibility increase, is revealed in the visibility measurement. To perform this measurement, we probe the axion port with a tone generated by a microwave generator and we discretely step it across the cavity resonance, measuring the visibility α at the measurement port.

Plotted in Fig. 2(d) is α^2 for the quantum limited and GC-enhanced cases. Given that spectral scan rate scales like $R \propto \int_{-\infty}^{\infty} \alpha^2 d\delta$, a scan-rate enhancement of 5.69 \pm 0.12 is extracted from the ratio of the areas enclosed by the α^2 curves, matching theoretical predictions given the experimentally determined interaction rates extracted from the scattering parameter measurements.

As demonstrated, the scan rate is enhanced by both the visibility-bandwidth increase and the peak-visibility improvement. The peak-visibility improvement arises from the fact that the potential axion signal is amplified before it passes through requisite lossy directional elements in the measurement chain, making it more robust to noise introduced by these lossy components. A more detailed discussion is included in Appendix A.

IV. ENHANCED SCAN RATE IN A SYNTHETIC AXION SEARCH

In a real axion search, the goal is to detect a signal that is spectrally broader and several orders of magnitude weaker than the probe tones used to measure visibility in Sec. III. The resolution or exclusion of such a weak signal at an unknown frequency requires integration for some time at each cavity tuning step to obtain a power spectrum and then combination of the power spectra obtained from many adjacent tuning steps [4]. In this section, we use the same measurement setup as described in Sec. III and we demonstrate that the GC-enhanced method still yields significant scan-rate enhancement when used to detect a weak synthetic axionlike tone.

To characterize the performance of the GC-enhanced detector in a more realistic search without addressing the added complexity of the magnetic field for axion-photon conversion, we instead inject synthesized fake axion, or "faxion," tones through the weakly coupled axion port to mimic how an axion signal would couple to a cavity in

the presence of a strong magnetic field. The faxion line shape is achieved by frequency modulating a microwave tone using voltages sampled randomly from a probability distribution which follows the predicted axion spectral distribution [25]. We calibrate the power in the faxion tone such that when it is resonant with the cavity mode, it appears at the measurement port with a peak PSD that is roughly 1% of the level of vacuum fluctuations when measured in the quantum limited mode of operation. Further details of the faxion line-shape generation are included in Appendix C.

To reduce technical complexity, we simulate the tuning of the cavity across a signal at a fixed but unknown frequency by instead tuning the faxion tone while keeping the cavity-mode frequency fixed, as illustrated by Fig. 3(a). The initial faxion frequency ω_{ax} is chosen randomly from within a 1-MHz initialization window outside of the axion-sensitive band of the cavity and the detector is blind to this initial choice. The tone is tuned in 10-kHz steps forward over a 26-MHz window that encompasses the full frequency range over which the cavity is axion

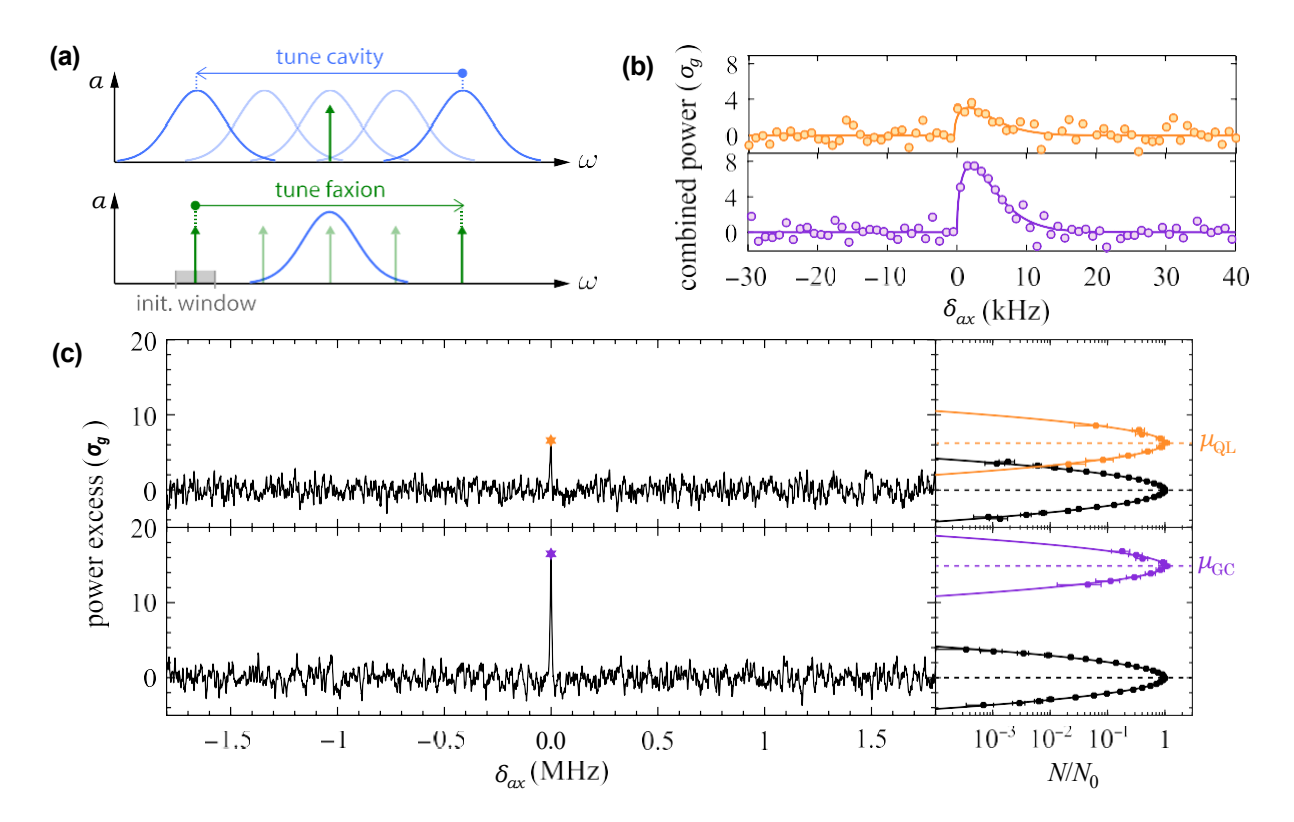


FIG. 3. The scan-rate enhancement in detecting a weak signal using the GC-enhanced method. (a) The tuning of the cavity frequency across an axion signal in a real search is simulated by tuning the faxion tone past a fixed-frequency cavity. (b) After combining the power spectra from all tuning steps, the faxion tone can be resolved above the level of noise with a spectral distribution that matches the line shape of the injected faxion tone, as given by the solid lines. The combined spectrum resulting from the quantum limited search is plotted in orange, while the spectrum from the GC-enhanced search is plotted in purple. (c) Left panels: grand spectra (black), with markers identifying the faxion bins in each case. Right panels: repeating the above process 210 times results in two faxion power-excess histograms, normalized to their peak counts N_0 and distributed around mean power excesses $\mu_{\rm QL}$ and $\mu_{\rm GC}$. A factor of 5.61_{\pm} 0.09 scan-rate enhancement is obtained from $(\mu_{\rm GC}/\mu_{\rm QL})^2$. The noise-power-excess histogram is plotted in black for comparison.

sensitive. At each faxion-tuning step, a power spectrum is acquired, resulting in a total of 2601 spectra. In the data processing, each spectrum is subsequently shifted backward in frequency by the amount the faxion has tuned from the fixed but unknown frequency ω_{ax} , such that the faxion tones all align at that frequency as if the cavity had been tuned across it [11].

Following the data-processing procedure established by prior haloscope experiments [11,25], we process the shifted spectra to produce a single combined spectrum that can be plotted as a function of the detuning δ_{ax} from the faxion frequency in each of the 2601 spectra. This results in a clear faxion-induced power excess, which follows the expected axion line shape closely, as plotted in Fig. 3(b). To further improve the SNR and resolve the faxioninduced power excess, maximum likelihood estimation is performed on the combined spectrum by accounting for the faxion line shape. This yields the grand spectrum. Sample grand spectra that result from operating the device in the quantum limited and GC-enhanced modes are plotted in Fig. 3(c), with the frequency bins most likely to contain the faxion-induced power excess marked by orange and purple stars.

To quantify the scan-rate enhancement from the weak signal search, we repeat this faxion injection and detection procedure 210 times with 210 randomly initialized faxion frequencies for both the quantum limited and GC-enhanced cases. In each case, the faxion bin power excesses from 210 grand spectra are added to a histogram [orange and purple points in the right panel of Fig. 3(c)], resulting in two distributions of faxion-induced power (solid lines). The right panel of Fig. 3(c) also displays the noise-power distribution (black) obtained from a single grand spectrum that is normally distributed with a mean value of zero and a standard deviation σ_g . A bin containing faxion-induced power is subject to the same noise fluctuations as the bins containing only noise but with a faxion-induced power excess that shifts the mean of the distribution away from zero. Therefore, after measurements of equivalent duration, the power in the faxion bins is normally distributed with standard deviation close to σ_g and means $\mu_{\rm QL} = 6.27 \pm 0.07$ (quantum limited) and μ_{GC} =14.85 $\stackrel{\frown}{\cancel{D}}$.06 (GC-enhanced). The SNR scales with the square root of the measurement time. Therefore, it would require a factor of the SNR squared $(\mu_{\rm GC}/\mu_{\rm OL})^2$ 5.61 times longer measurement time for the quantum limited case to achieve a signal distribution that has the same mean excess as does the GC-enhanced distribution, signifying a factor of 5.61+0.09 scan-rate enhancement.

Although the JRM here is not optimized for Kerr-free operation [20,26–28], we note that the scan-rate limitation is not higher-order parametric processes that might limit the scan-rate enhancement to far below the demonstrated value. The most readily understood higher-order effect is

single-mode squeezing induced by the fourth-order interaction of the JRM, which causes amplified measurement noise and reduced transmission gain when both the swapping and two-mode squeezing drives are present. We discover that these effects can be compensated by detuning the pump frequencies away from their nominal optimal values. A more detailed discussion of this compensation procedure will be included in a future publication [29].

Rather than originating from higher-order parametric processes, the scan-rate limitation in the GC mode of operation actually takes the form of difficulty with increasing the interaction rates further while maintaining unit reflected measurement noise. We observe that when operating the GC amplifier with $g_C/2\pi = g_G/2\pi \approx 7$ MHz, the operating point drifts over the course of several minutes, causing amplified measurement noise. These drifts could be compensated by applying shifts on the order of 10 kHz to the applied pump frequencies to return to the point of optimal operation. We suspect these drifts to be caused by mode frequency shifts away from the applied pumps, possibly resulting from fluctuations in the flux threading the JRM loop. The sensitivity of the GC operating point to such drifts makes it challenging to tune up to a point of higher interaction rates than are achieved.

V. FURTHER IMPROVEMENT FROM IMBALANCED ENTANGLEMENT AND SWAPPING

Although it should be possible to achieve higher balanced GC interaction rates with an active feedback loop to prevent the operating point from drifting, here we implement a simpler strategy. Imbalancing the rates slightly such that g_C 2: g_G makes the amplifier performance less sensitive to shifts in the mode frequencies, making it possible to operate with increased interaction rates, a wider visibility bandwidth, and consequently a greater scanrate enhancement. Under GC-imbalanced (GCI) operation [13,14], the measurement noise decreases on resonance, rather than being unit reflected over the entire bandwidth, as shown in Fig. 4(a). Operating our device at a GCI point with $g_C/2\pi = 12.25 + 0.01$ MHz $> g_G/2\pi =$ 11.76 ± 0.01 MHz enables a scan-rate enhancement of 8.17 +0.16, as demonstrated in Fig. 4(b). While the imbalanced operation itself yields a slight improvement in scan rate relative to a balanced operating point [12–14], the primary benefit of operating in this imbalanced way is the increased interaction rates.

Although the interaction rates may be increased further beyond this point by pumping more strongly, additional scan-rate enhancement is not achieved. With stronger pumps, we observe that the visibility drops to below the level of the quantum limited peak visibility, indicating that the amplification induced by the JPC is no longer noiseless. This could be caused by heating from the strong applied

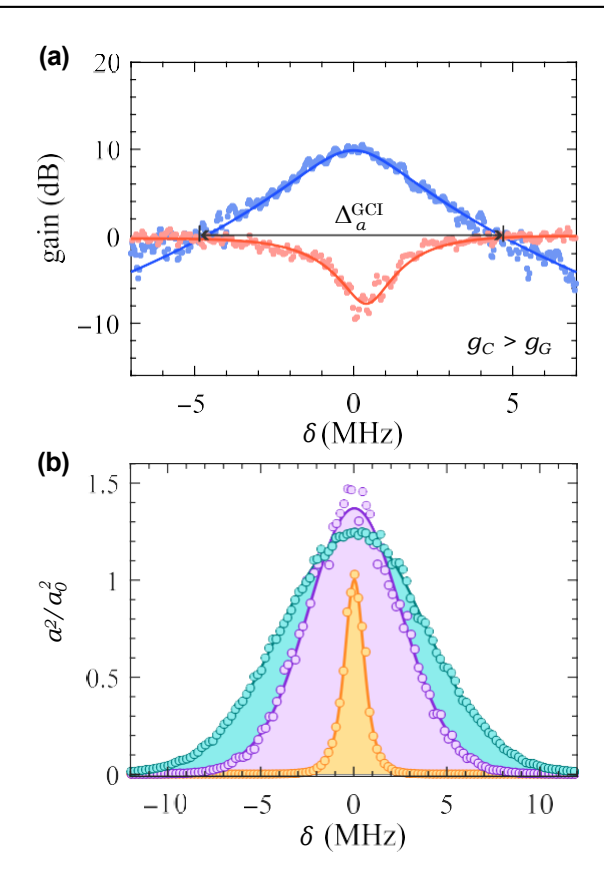


FIG. 4. An experimental demonstration of GC-imbalanced (GCI) operation. (a) The gain of the cavity and measurement noise under the GCI operation. We extract interaction rates of $gc/2\pi = 12.25 \pm 0.01$ MHz $> g_G/2\pi = 11.76 \pm 0.01$ MHz from the fits, corresponding to a visibility bandwidth that is larger than the GC bandwidth $L'l_G^{GCI} > L'l_G^{GC}$. (b) The visibility squared for the GCI case (teal) relative to the GC and quantum limited cases. A scan-rate enhancement of 8.17 ± 0.16 is extracted in the GCI case relative to the quantum limited case.

pumps or by undesired higher-order parametric processes that are not included in our model but contribute more strongly as the pump-induced current across the junctions approaches the critical current.

To reduce the contribution of these higher-order processes, one could tesselate three-wave-mixing dipole elements (SNAILs) on the arms of the JRM [30]. Alternatively, application of the entanglement interaction between the readout mode and a third ancilla mode (at a different frequency) rather than the cavity mode [31] would eradicate some of the higher-order parametric processes that may limit the performance. However, even without optimizing the three-wave mixing element, we predict, using our visibility model (Appendix A), that maintaining the demonstrated GCI interaction rates and all of the other experimental parameters the same but assuming a reduced cavity-mode loss rate equal to that of a typical copper haloscope cavity [10] ($\kappa p 2\pi \pm 100 \text{ kHz}$) would result in a scan-rate enhancement of a factor of 20.

VI. CONCLUSION AND OUTLOOK

The quantum enhanced sensing technique demonstrated in this experiment would accelerate an axion search by allowing for fewer total tuning steps or, equivalently, for shorter integration time at any given step while achieving the same confidence to resolve or exclude a signal. The next steps toward implementation will involve coupling a microwave cavity immersed in a magnetic field that enables axion-photon conversion to the three-wavemixing element. Because the superconducting circuitry will need to be spatially separated from the magnetic field, the primary challenge will be to achieve sufficient coupling between the cavity and the three-wave mixing element mediated through a transmission line. The transmission line will introduce standing-wave modes and undesired interactions between the readout mode and these standingwave modes will need to be mitigated in order to realize a significant scan-rate enhancement [12]. The mitigation of these interactions should be possible either by using a variable-length transmission line [12] or by implementing a variation on the GC-enhanced technique that makes use of a third ancilla mode [31,32]. With these optimizations, the implementation of this quantum enhanced technique in a real axion search would mark a significant step toward the feasibility of a comprehensive search of the axion parameter space.

ACKNOWLEDGMENTS

We thank the Devoret group at Yale University for use of their device. We additionally thank Daniel Palken and Benjamin Brubaker for helpful discussions. This document was prepared with support from the resources of the Fermi National Accelerator Laboratory (Fermilab), the U.S. Department of Energy, the Office of Science, and the High Energy Physics (HEP) User Facility. Fermilab is managed by Fermi Research Alliance, LLC (FRA), acting under Contract No. DE-AC02-07CH11359. Additionally, this work was supported by Q-SEnSE: Quantum Systems through Entangled Science and Engineering [National Science Foundation (NSF) Quantum Leap Challenge Institutes (QLCI) Award No. OMA-2016244] and the NSF Physics Frontier Center at JILA (Grant No. PHY-1734006).

APPENDIX A: SCATTERING PARAMETERS AND VISIBILITY THEORY

In this appendix, we describe the full theoretical model that is used to derive the fits in Figs. 2 and 4 and we present an explanation for why the GC-enhanced technique improves the peak visibility of a haloscope by accounting for losses in the measurement chain. We begin with a Hamiltonian that includes the pure two-mode squeezing and state-swapping interactions \hat{H} GC as well as the

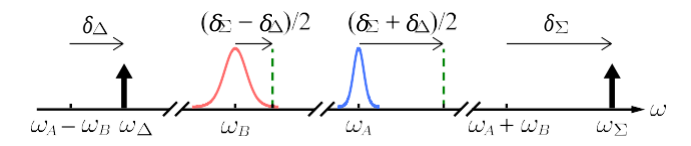


FIG. 5. The frequency diagram for the modes, pumps, and detunings. The pump tones are applied with some detunings δ_{L7} and $\delta_{:E}$ with respect to the difference and sum frequencies of the Kerr-shifted cavity and readout mode frequencies ($\omega_{A,B}$) and are plotted using black arrows. The Hamiltonian is written in the rotating frame of the half-pump frequencies as labeled by dashed green lines for each mode. The rotating frames for the cavity and readout modes are at frequencies ($\omega_{:E} - \omega_{L7}$)/2 = $\omega_B + (\delta_{:E} - \delta_{L7}$)/2 and ($\omega_{:E} + \omega_{L7}$)/2 = $\omega_A + (\delta_{:E} + \delta_{L7}$)/2 respectively.

undesired single-mode squeezing interactions \hat{H} _{SMS} and compensatory pump detunings \hat{H} _{det}. We write the Hamiltonian \hat{H} \hat{H} _{det+ \hat{H} _{GC+ \hat{H} _{SMS} in the frame of the "half-pump" frequencies $(\omega_{:E}+\omega_{L}\eta)/2$ for the cavity mode (A) and $(\omega_{:E}-\omega_{L}\eta)/2$ for the readout mode (B) after the rotating-wave approximation as}}

$$\hat{H}_{\text{det}} = -\frac{\delta_{:E} + \delta_{LI}}{2} \hat{A}^{\dagger} \hat{A}^{\dagger} + \frac{1}{2} - \frac{\delta_{:E} - \delta_{LI}}{2} \hat{B}^{\dagger} \hat{B}^{\dagger} + \frac{1}{2} ,$$

$$\hat{H}_{GC} = g_{C} \hat{A}^{\dagger} \hat{B}^{\dagger} + g_{G} e^{-i\phi} \hat{A}^{\dagger} \hat{B}^{\dagger} + \text{h.c.},$$

$$\hat{H}_{SMS} = \frac{1}{2} s_{A} e^{-i\phi} \hat{A}^{\dagger 2} + \frac{1}{2} s_{B} e^{-i\phi} \hat{B}^{\dagger 2} + \text{h.c.},$$
(A1)

where the annihilation and creation operators \hat{A} , \hat{B} , \hat{A} , and \hat{B} are slowly varying envelopes, s_A and s_B are the single-mode squeezing rates for each mode, $\delta_{:E}$ and δ_{LT} describe pump detunings from the sum and difference frequencies of the Kerr-shifted modes ($\omega_{:E} = \omega_A + \omega_B + \delta_{:E}$ and $\omega_{LT} = \omega_A - \omega_B + \delta_{LT}$), and the phase ϕ is set by the phase difference between the state-swapping and two-mode squeezing drives. These pump frequencies and detunings can be visualized in Fig. 5.

From this Hamiltonian, the Heisenberg-Langevin equations can be written as

$$\dot{\hat{A}} = i \frac{\delta_{:E} + \delta_{LT}}{2} - \frac{\kappa_a + \kappa_f}{2} \hat{A} - i s_A e^{-i\phi} \hat{A}^{\dagger}
- i g_C \hat{B} - i g_G e^{-i\phi} \hat{B}^{\dagger} + \sqrt{\kappa_a} \hat{A}_{a,in} + \sqrt{\kappa_f} \hat{A}_{f,in},
\dot{\hat{B}} = i \frac{\delta_{:E} - \delta_{LT}}{2} - \frac{\kappa_m}{2} \hat{B}^{\hat{}} - i s_B e^{-i\phi} \hat{B}^{\dagger}
- i g_C \hat{A} - i g_G e^{-i\phi} \hat{A}^{\dagger} + \sqrt{\kappa_m} \hat{B}_{m,in}.$$
(A2)

By solving these equations in the frequency domain, together with the input-output theory relations given by [33]

$$\hat{A}_{i,\text{out}} = \hat{A}_{i,\text{in}} - \sqrt{\kappa_i} \hat{A}, (i = a, f)$$

$$\hat{B}_{m,\text{out}} = \hat{B}_{m,\text{in}} - \sqrt{\kappa_m} \hat{B}, \qquad (A3)$$

we calculate the scattering parameters S_{jk} between ports k and j.

We use these scattering parameters as fits in Figs. 2(b), 2(c), and 4(a). In each of the fits, the interaction rates g_C and g_G are extracted as fitting parameters. In the quantum limited case, the single-mode squeezing rates and pump detunings are set to zero, because operating with only the state-swapping interaction enabled does not induce singlemode squeezing from the quartic nonlinearities. Therefore, the optimal pump frequency is $\omega_{L'l} = \omega_A - \omega_B$. Nevertheless, any unintentional pump detuning δ_{LT} would shift the frequency at which unit transmission occurs [defined as $\delta = 0$ in Fig. 2(b)] to $\omega_B + \delta_L \sqrt{2}$. In the GC case, the cavity and readout single-mode squeezing rates are set to 7% and 14% of the GC interaction rates, respectively, and in the GCI case, they are set to 12% and 20% of the GCI state-swapping rate. These fractions are determined from the ratio of the quartic nonlinear coefficient to the cubic coefficient in the JRM Hamiltonian [17,34], which is set by the parameters of the JPC circuit. In both the GC and the GCI modes of operation, the detunings δ_{LT} and $\delta_{:E}$ are chosen to optimally compensate the effects of the singlemode squeezing, $\delta_{L7} = -s_A - s_B$ and $\delta_{:E} = -s_A + s_B$, as

From these scattering parameters, we calculate the PSD that would be induced by an axion signal S_a as well as the noise PSD S_N at the measurement port of the JPC [12]. Taking the ratio of these two quantities yields the visibility in the absence of any imperfections in the measurement chain. At the output of the JPC, the peak visibility should be the same in both the GC-enhanced and quantum limited cases, provided that the GC gain is large enough that the cavity noise is the dominant source of noise on resonance [12].

will be discussed in a future publication [29]. Because of

these detunings, the frequency at which peak transmission

gain occurs [defined as $\delta = 0$ in Figs. 2(c) and 4(a)] is

 $\omega_B + (\delta_{:E} - \delta_{L'l})/2$.

However, because the signal must also pass through the lossy and imperfect measurement chain, we find that the GC-enhanced technique actually improves the peak visibility of a haloscope. As displayed in Fig. 6, we model the loss between the JPC and the JPA as a beam splitter that allows quantum noise comprising thermal and vacuum fluctuations to enter, polluting the signal. In GC operation, the signal is amplified noiselessly by the JPC before it encounters noise entering from this channel. Therefore, it is more robust to this noise than an unamplified signal measured in the quantum limited case would be.

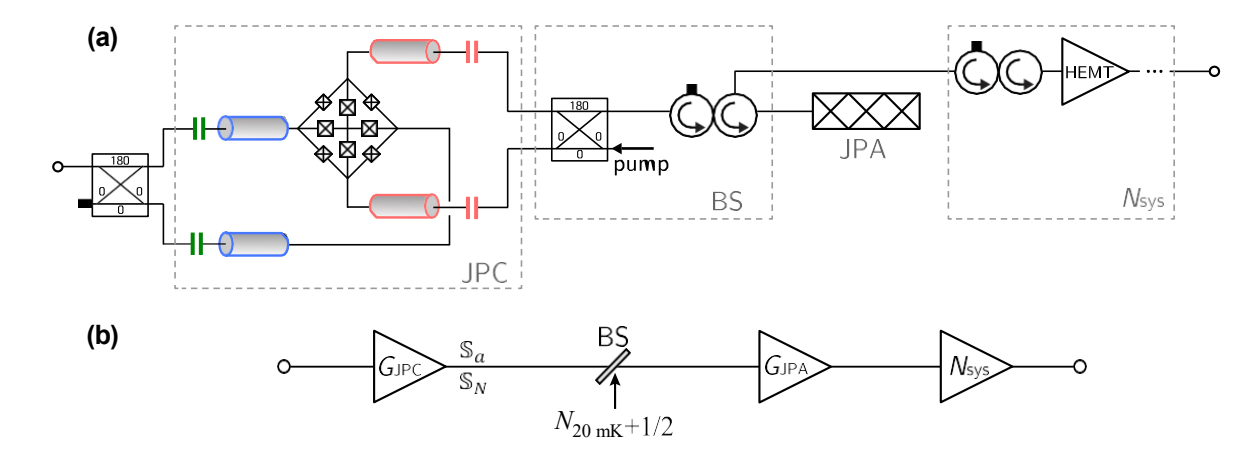


FIG. 6. (a) A simplified microwave network diagram of the experimental setup. The lossy microwave elements between the JPA and the JPC are modeled as a beam splitter (BS). (b) The outgoing fields from the JPC, S_a and $S_{N,meas}$, are polluted by thermal and vacuum noise, which enters at the lossy directional elements modeled by the beam splitter, resulting in the decrease of peak visibility.

To model this effect, we write the total noise PSD measured at the output of the measurement chain referred to the output of the JPC as

$$S_{N,\text{meas}}(\omega) = S_{N}(\omega) + \frac{1-\eta}{\eta} N_{20 \text{ mK}}(\omega) + \frac{1}{2} + \frac{N_{\text{sys}}}{\eta G_{\text{JPA}}(\omega)}, \tag{A4}$$

where S_N comprises cavity noise and measurement noise and has an analytical expression given by Eq. (14) of Ref. [12]. Here, N_{20} mk $(e^{n\omega/k_BT}-1)^{-1}$ is the Bose occupancy at the fridge base temperature of T=20 mK and the added half quanta in Eq. (A4) comes from vacuum fluctuations. The measured phase-sensitive gain of the JPA as a function of frequency is given by $G_{\rm JPA}(\omega)$ and $N_{\rm sys}$ =32 quanta is the total noise added by the system after the JPA. Finally, the energy-transmission efficiency of the beam-splitter interaction η , as modeled in Fig. 6, is left as a fit parameter.

As both the JPC and the JPA are operated phase sensitively, we assume that they do not add noise in their measurement of a single quadrature of the signal [1]. The visibility as measured at the measurement port is then given by

$$\alpha(\omega) = S_a/S_{N,\text{meas}}(\omega)$$
 (A5)

and the visibility fits in Figs. 2(d) and 4(b) are obtained from Eqs. (A4) and (A5). From fitting the visibility data displayed in Fig. 2(d), we extract η =0.9. We note, however, that if the JPC is not completely noiseless in the strongly pumped GC regime, as is assumed, then the extracted value for η can be an overestimation. Any overestimation of η would have a negligible effect on the

measured scan-rate enhancement, however, as the JPC added noise would compensate for this effect.

APPENDIX B: EXPERIMENTAL SETUP

The full experimental setup is presented in Fig. 7, including the room-temperature control electronics. In this

appendix, we trace the path of a faxion signal through the experiment and describe how various experimental parameters are measured and extracted. The faxion tone is first generated by a room-temperature microwave generator (Keysight E8257D) and frequency modulated to resemble the axion line shape by an arbitrary waveform generator (AWG). The tone is directed by a cryogenic circulator toward the L'l port of an off-chip 180° hybrid coupler connecting the north-south lines of the JPC.

The JPC is attached to the bottom plate of a dilution refrigerator, which is at 20 mK. It is biased via an external coil that is connected to a dc-current source (Yokogawa GS200) at room temperature. The coil generates a dc magnetic field threading the JRM loop and the chipcoil ensemble is magnetically shielded with aluminum and Cryoperm. The dc bias point in this experiment is chosen to provide strong three-wave mixing capability such that optimal interaction rates can be achieved [34].

Two off-chip 180° hybrid couplers connect the north-south and east-west lines of the JPC. The cavity mode is accessed via the L'l port of the north-south hybrid coupler (right) and the readout mode is accessed via the L'l port of the east-west hybrid coupler (left). The coupling rate κ_a and the internal loss rate κ_f of the cavity mode are extracted from a nonlinear fit to the measured scattering parameter of the JPC in reflection off the axion port $S_{aa}(\delta)$ with the pumps off. The measurement port coupling rate κ_m is extracted in the same way by measuring the scattering parameter off the measurement port $S_{mm}(\delta)$.

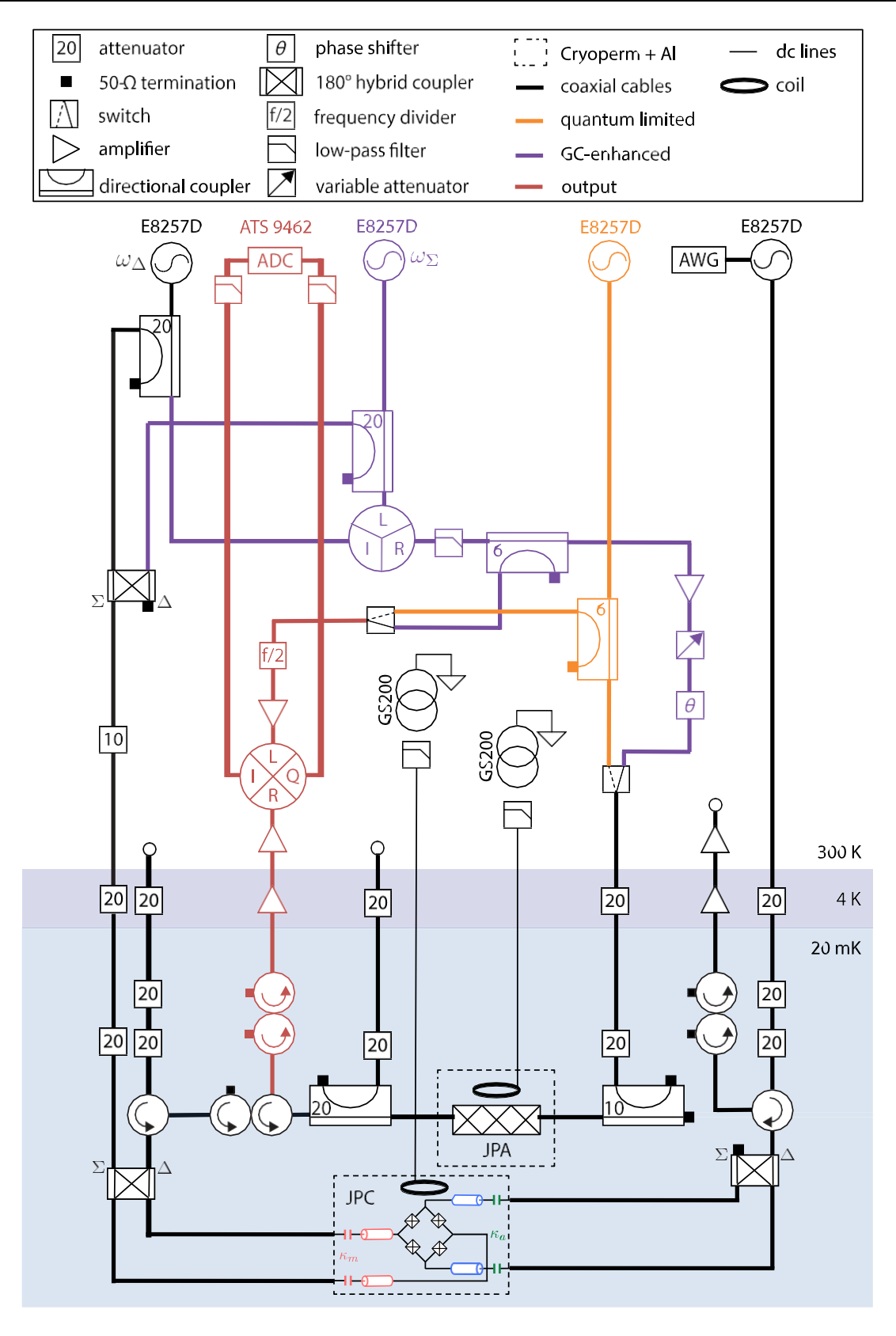


FIG. 7. A full schematic of the GC-enhanced proof-of-principle demonstration experiment, including the room-temperature control electronics. Coaxial cables are in bold. The thinner lines represent dc cables. Components required for operating the device in a quantum limited manner are in orange, while components used in the GC-enhanced mode are in purple. Output lines and components are in red. The lines terminated in ports can be used (from left to right) to probe the readout mode, to probe the JPA, and to measure out of the cavity mode. These ports are used to characterize device performance [Figs. 2(b) and 2(c)] but are not actively used in the visibility measurement or weak signal search. Shunt junctions of the JPC are not depicted.

These rates depend on the dc bias point of the JRM and they are measured at the operational bias point used in the experiment. The main source of uncertainty in these measurements is statistical error caused by added noise from the measurement chain, particularly from the first noisy amplifier, which is the HEMT at 4 K.

In the visibility measurement and faxion search, the device is pumped through the :E port of the east-west hybrid, accessing the common mode of the JRM, while the :E port of the other hybrid is terminated with a 50-Q termination. In both the quantum limited and GC-enhanced modes of operation, the device is pumped at ω_{LT} by a microwave generator to enable the swap interaction. In the GC-enhanced case, this pump tone is combined using a hybrid coupler at 300 K with an additional two-mode squeezing pump tone at frequency $\omega_{:E}$ generated by another microwave generator (purple).

Upon being converted (and amplified in the GCenhanced case) from the cavity mode to the readout mode, the tone passes through the L'l port of the east-west hybrid coupler and is directed by a circulator toward the measurement chain. It passes through two circulators used to isolate the JPC from JPA backaction, as well as a directional coupler that enables probing of the JPA for gain calibration. The JPA is also attached to the bottom plate of the dilution refrigerator. Like the JPC, it is biased via an external coil connected to a dc current source and it is also magnetically shielded with aluminum and Cryoperm. In the quantum limited case, the JPA is pumped using a fourth microwave generator (orange). In the GC-enhanced case, the $\omega_{:E}$ and ω_{LT} pump tones are combined using a three-port mixer (purple) to yield a pump tone at $2\omega_A$. This method of generating the JPA pump tone from the JPC pumps spontaneously phase locks the JPA to the JPC. In both the quantum limited and GC cases, the pump tones are then passed through directional couplers (orange and purple) that direct a fraction of the pump tones to be used to generate the local oscillator of a four-port mixer. In the GC case, the remainder of the pump tone is amplified and then passed through a manually controlled variable attenuator, used to control the power in the pump tone and the resulting JPA gain. It also passes through a manual phase shifter, used to align the JPC and JPA amplified quadratures. The manual act of switching between the quantum limited and GC modes of pumping is schematically represented by the switch symbols in Fig. 7. Finally, the pump tone passes through a 10-dB directional coupler and couples to the pump port of the JPA.

After amplification from the JPA, outgoing fields are routed back through the directional coupler and circulators (red) toward the next-stage amplifier (a HEMT at 4 K). After the HEMT, they are amplified further by a room-temperature MITEQ amplifier and enter an in-phase and quadrature (IQ) mixer (red) at the rf port. The local oscillator of the mixer is supplied by a fraction of the

JPA pump tone which is frequency divided ($\omega_0 = \omega_p / 2$) and amplified. After being mixed down, the in-phase and quadrature signals are directed into dc-11 MHz low-pass filters and then finally digitized by an analog-to-digital converter (ADC).

APPENDIX C: SYNTHETIC AXION GENERATION AND DATA PROCESSING

To produce the synthetic faxion tones, we generate a list of voltage samples drawn randomly from a cumulative distribution function (CDF) derived from the axion line shape [25] and we use the list of voltage samples to frequency modulate a microwave tone. We sample from the CDF to update the faxion frequency at a rate of 1.5 kHz, much slower than the modulation depth, which is set to 30 kHz. Meanwhile, the measurement rate at each step (2.4 mHz) is much slower than either of these rates. This means that at any given measurement step, the faxion frequency is updated many times over the course of the integration time, resulting in a signal with a shape that mimics the axion line shape.

An ADC (ATS9462) continuously records the in-phase and quadrature streams exiting the IQ mixer over the course of 0.16 s. This time-domain trace is divided into n = 32 subtraces with acquisition time $\tau_{aq} = 5$ ms each. Each subtrace is subsequently Fourier transformed, yielding PSDs at positive frequencies (ω) that describe detunings from the local-oscillator (LO) frequency. The PSDs at these positive frequencies are subsequently assigned to their negative-frequency ($-\omega$) counterparts in the rf. This produces a spectrum that is symmetric about the LO frequency. The 32 transformed and symmetrized subtraces are then averaged together to produce a single power spectrum, called the "raw spectrum," which has a frequency-dependent profile. This process is repeated at every faxion-tuning step over the 26-MHz range, resulting in 2601 raw spectra.

In order to identify any power excesses in the data, it is useful to remove the base frequency-dependent profile. To do so, we average the 2601 raw spectra together to get an averaged baseline and we filter the baseline with a Savitzky-Golay filter to remove all of the small-scale structure from it (features comparable to the axion linewidth and narrower), such that all faxion-induced structure would be removed. Then, each raw spectrum is divided by the filtered baseline to remove the frequency-dependent profile while preserving the faxion-scale structure. Subtracting 1 from these spectra results in 2601 power-excess spectra, which have mean 0 and standard deviation close to $n\tau_{aq}L'l_v$, where $L'l_v = 200$ Hz is the resolution bandwidth in our measurement.

The 2601 spectra are then shifted in 10-kHz increments such that the faxion tone in each spectrum lines up with its random initial frequency. This simulates the tuning of a

cavity across a fixed-frequency axion tone in a real axion search. Each of the 2601 shifted spectra is then rescaled by the normalized visibility $\alpha(\omega)$ so that frequency bins with higher sensitivity to the faxion are weighted more. The rescaled spectra are then added together to produce a single combined spectrum with mean 0 and standard deviation close to 1, which has a faxion-induced power excess that contains contributions from all of the axionsensitive frequencies. This procedure results in a clear faxion-induced power excess, which follows the expected axion line shape closely, as demonstrated in Fig. 3(b). To further improve the SNR and determine the frequency bin most likely to contain the faxion, we perform maximum likelihood estimation on the combined spectrum, accounting for the faxion line shape, which results in the grand spectrum displayed in Fig. 3(c), with the faxion-induced power excesses marked.

- [1] C. M. Caves, Quantum limits on noise in linear amplifiers, Phys. Rev. D **26**, 1817 (1982).
- [2] M. Tse, H. Yu, N. Kijbunchoo, A. Fernandez-Galiana, P. Dupej, L. Barsotti, C. D. Blair, D. D. Brown, S. E. Dwyer, and A. Effler, *et al.*, Quantum-Enhanced Advanced LIGO Detectors in the Era of Gravitational-Wave Astronomy, Phys. Rev. Lett. 123, 231107 (2019).
- [3] A. Bienfait, J. J. Pla, Y. Kubo, M. Stern, X. Zhou, C. C. Lo, C. D. Weis, T. Schenkel, M. L. W. Thewalt, and D. Vion, *et al.*, Reaching the quantum limit of sensitivity in electron spin resonance, Nat. Nanotechnol. 11, 253 (2016).
- [4] B. M. Brubaker, L. Zhong, Y. V. Gurevich, S. B. Cahn, S. K. Lamoreaux, M. Simanovskaia, J. R. Root, S. M. Lewis, S. Al Kenany, and K. M. Backes, *et al.*, First Results from a Microwave Cavity Axion Search at 24 μmeV, Phys. Rev. Lett. 118, 061302 (2017).
- [5] P. Sikivie, Detection rates for "invisible"-axion searches, Phys. Rev. D 32, 2988 (1985).
- [6] Richard Bradley, John Clarke, Darin Kinion, Leslie J Rosenberg, Karl van Bibber, Seishi Matsuki, Michael Mück, and Pierre Sikivie, Microwave cavity searches for dark-matter axions, Rev. Mod. Phys. 75, 777 (2003).
- [7] D. A. Palken, Ph.D. thesis, University of Colorado Boulder, 2020.
- [8] A. R. Zhitnitsky, On possible suppression of the axion-hadron interactions, Sov. J. Nucl. Phys. **31**, 260 (1980).
- [9] M. Dine, W. Fischler, and M. Srednicki, A simple solution to the strong CP problem with a harmless axion, Phys. Lett. B 104, 199 (1981).
- [10] K. M. Backes, D. A. Palken, S. Al Kenany, B. M. Brubaker, S. B. Cahn, A. Droster, Gene C. Hilton, Sumita Ghosh, H. Jackson, and S. K. Lamoreaux, *et al.*, A quantum enhanced search for dark matter axions, Nature **590**, 238 (2021).
- [11] M. Malnou, D. A. Palken, B. M. Brubaker, Leila R. Vale, Gene C. Hilton, and K. W. Lehnert, Squeezed Vacuum Used to Accelerate the Search for a Weak Classical Signal, Phys. Rev. X 9, 021023 (2019).

- [12] K. Wurtz, B. M. Brubaker, Y. Jiang, E. P. Ruddy, D. A. Palken, and K. W. Lehnert, Cavity Entanglement and State Swapping to Accelerate the Search dor Axion Dark Matter, PRX Quantum 2, 040350 (2021).
- [13] O. Lanes, Ph.D. thesis, University of Pittsburgh, 2020.
- [14] A. Metelmann, O. Lanes, T-Z. Chien, A. McDonald, M. Hatridge, and A. A. Clerk, Quantum-limited amplification without instability (2022), ArXiv:2208.00024.
- [15] B. Abdo, A. Kamal, and M. Devoret, Nondegenerate threewave mixing with the Josephson ring modulator, Phys. Rev. B 87, 014508 (2013).
- [16] A. Roy and M. Devoret, Introduction to parametric amplification of quantum signals with Josephson circuits, C. R. Phys. 17, 740 (2016).
- [17] N. Bergeal, R. Vijay, V. E. Manucharyan, I. Siddiqi, R. J. Schoelkopf, S. M. Girvin, and M. H. Devoret, Analog information processing at the quantum limit with a Josephson ring modulator, Nat. Phys. 6, 296 (2010).
- [18] N. Bergeal, F. Schackert, M. Metcalfe, R. Vijay, V. E. Manucharyan, L. Frunzio, D. E. Prober, R. J. Schoelkopf, S. M. Girvin, and M. H. Devoret, Phase-preserving amplification near the quantum limit with a Josephson ring modulator, Nature 465, 64 (2010).
- [19] A. Metelmann and A. A. Clerk, Phys. Rev. X 5, 021025 (2015).
- [20] T.-C. Chien, O. Lanes, C. Liu, X. Cao, P. Lu, S. Motz, G. Liu, D. Pekker, and M. Hatridge, Multiparametric amplification and qubit measurement with a Kerr-free Josephson ring modulator, Phys. Rev. A 101, 042336 (2020).
- [21] T. Yamamoto, K. Inomata, M. Watanabe, K. Matsuba, T. Miyazaki, W. D Oliver, Y. Nakamura, and J. S. Tsai, Flux-driven Josephson parametric amplifier, Appl. Phys. Lett. 93, 042510 (2008).
- [22] M. A. Castellanos-Beltran, K. D. Irwin, G. C. Hilton, L. R. Vale, and K. W. Lehnert, Amplification and squeezing of quantum noise with a tunable Josephson metamaterial, Nat. Phys. 4, 929 (2008).
- [23] R. Vijay, D. H. Slichter, and I. Siddiqi, Observation of Quantum Jumps in a Superconducting Artificial Atom, Phys. Rev. Lett. 106, 110502 (2011).
- [24] M. Hatridge, R. Vijay, D. H. Slichter, John Clarke, and I. Siddiqi, Dispersive magnetometry with a quantum limited SQUID parametric amplifier, Phys. Rev. B 83, 134501 (2011).
- [25] B. M. Brubaker, L. Zhong, S. K. Lamoreaux, K. W. Lehnert, and K. A. van Bibber, HAYSTAC axion search analysis procedure, Phys. Rev. D **96**, 123008 (2017).
- [26] V. V. Sivak, N. E. Frattini, V. R. Joshi, A. Lingenfelter, S. Shankar, and M. H. Devoret, Kerr-Free Three-Wave Mixing in Superconducting Quantum Circuits, Phys. Rev. Appl. 11, 054060 (2019).
- [27] N. E. Frattini, V. V. Sivak, A. Lingenfelter, S. Shankar, and M. H. Devoret, Optimizing the Nonlinearity and Dissipation of a SNAIL Parametric Amplifier for Dynamic Range, Phys. Rev. Appl. 10, 054020 (2018).
- [28] A. Miano, G. Liu, V. V. Sivak, N. E. Frattini, V. R. Joshi, W. Dai, L. Frunzio, and M. H. Devoret, Frequency-tunable Kerr-free three-wave mixing with a gradiometric snail, Appl. Phys. Lett. 120, 184002 (2022).

- [29] Y. Jiang, E. P. Ruddy, N. E. Frattini, K. O. Quinlan, and K. W. Lehnert, Single-mode squeezing compensation with pump detunings. *In preparation*.
- [30] N. E. Frattini, U. Vool, S. Shankar, A. Narla, K. M. Sliwa, and M. H. Devoret, 3-wave mixing Josephson dipole element, Appl. Phys. Lett. 110, 222603 (2017).
- [31] X. Li, M. Goryachev, Y. Ma, M. E. Tobar, C. Zhao, R. X Adhikari, and Y. Chen, Broadband sensitivity improvement
- via coherent quantum feedback with PT symmetry (2020), ArXiv:2012.00836.
- [32] Yifan Chen, Minyuan Jiang, Yiqiu Ma Jing Shu, and Yuting Yang, Axion haloscope array with *PT* symmetry, Phys. Rev. Res. 4, 023015 (2022).
- [33] D. F. Walls and G. J. Milburn, *Quantum Optics* (Springer-Verlag, Berlin, 2008).
- [34] Emmanuel Flurin, Ph.D. thesis, Ecole normale supérieure (ENS), Paris, 2014.